Size effects in microstructured superconductors and quantum materials

Fermin, R.

Citation

Fermin, R. (2022, December 7). *Size effects in microstructured superconductors and quantum materials*. *Casimir PhD Series*. Retrieved from https://hdl.handle.net/1887/3492762

STRONGLY CORRELATED RUTHENIUM OXIDE MICROSTRUCTURES

3

6

UNIVERSAL SIZE-DEPENDENT NONLINEAR CHARGE TRANSPORT IN SINGLE CRYSTALS OF THE MOTT INSULATOR Ca_2RuO_4

R. Fermin[*], G. Avallone[*], K. Lahabi, V. Granata, R. Fittipaldi, C. Cirillo, C. Attanasio, A. Vecchione & J. Aarts

The surprisingly low current density required for inducing the insulator-to-metal transition has made Ca_2RuO_4 an attractive candidate material for developing Mott-based electronics devices. However, the mechanism driving the resistive switching remains a controversial topic in the field of strongly correlated electron systems. In this chapter, we probe an uncovered region of phase space by studying high-purity Ca_2RuO_4 single crystals, using the sample size as the principal tuning parameter. Upon reducing the crystal size, we find a four orders of magnitude increase in the current density required for driving Ca_2RuO_4 out of the insulating state into a non-equilibrium (also called metastable) phase, which is the precursor to the fully metallic phase. By integrating a microscopic platinum thermometer and performing thermal simulations, we gain insight into the local temperature during simultaneous application of current and establish that the size dependence is not a result of Joule heating. The findings suggest an inhomogeneous current distribution in the nominally homogeneous crystal. Our study calls for a reexamination of the interplay between sample size, charge current, and temperature in driving Ca_2RuO_4 towards the Mott insulator-to-metal transition.

This chapter is based on the paper published in *npj Quantum Materials* **6**, 91 (2021).

[*] These authors contributed equally to this study

6.1. INTRODUCTION

The 4*d* electron Mott insulator Ca_2RuO_4[1] has become the subject of intense research in recent years due to its intriguing electrical [2, 3, 3–14] and magnetic properties[15, 16]. These range from a paramagnetic insulating phase at room temperature to ferromagnetism below 30 K under applied pressure[3], and a superconducting transition at ~0.4 K[2]. However, its most remarkable feature is arguably its current-driven insulator-to-metal transition (IMT) which occurs at unusually low electric field or current density thresholds (~ 40 V/cm or few A/cm^2 respectively)[17, 18]. This is in contrast to previous reports on Mott insulators, where the IMT is limited to low temperatures and/or to the application of high *E*-fields[19, 20]. The capacity to switch between resistive states at room temperature is a desirable property to realize current switchable memories, neuromorphic devices, and next-generation oxide electronics[21, 22].

The underlying mechanism responsible for such low current densities is still a topic of intense debate, as the driving force behind the IMT is not limited by the application of current. Due to its high resistivity in the insulating state, Joule heating plays a sig-

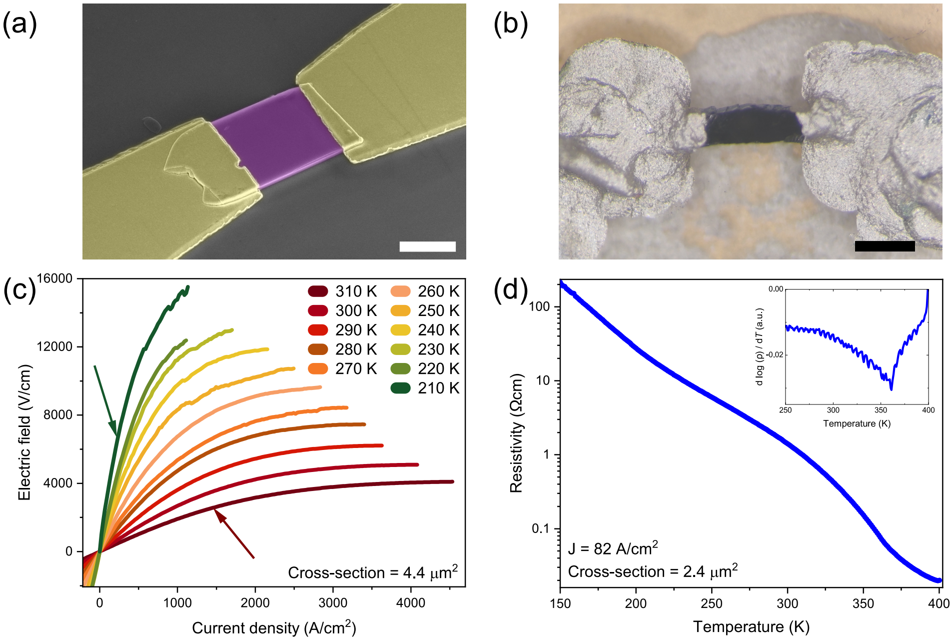

Figure 6.1: (a) Displays a false colored scanning electron micrograph of a microscopic sample (in purple) that is contacted by yellow colored Ti/Au contacts. The scale bar represents 0.3 μm. (b) Shows an optical microscope image of an mm-sized sample, where the scale bar measures 500 μm. Panel (c) shows *JE*-characteristics acquired on a microscopic sample at different temperatures. The arrows indicate the current density that corresponds to the Figure of Merit. Note that these curves are obtained below the IMT. The resistivity versus temperature of a typical microscopic sample is shown in panel (d). In the microscopic size range, we do not observe a sharp temperature-induced IMT. However, as indicated by the inset (the derivative of the curve in the main Figure), there is a clear inflection point indicating the thermal transition.

nificant role since the IMT can also be thermally driven by heating the crystal above 357 K[8]. This has led to ambiguity about the origin of the IMT, and whether it is thermally or electronically driven, as evident by the large number of works discussing local heating[7, 18, 23–27]. Specifically, in a recent work, it was found that the IMT is always accompanied by a local temperature increase to the transition temperature[23]. Moreover, as a precursor to the metallic phase, a third and non-equilibrium (also called metastable) phase has been detected by X-ray, neutron diffraction experiments, and additionally with Raman spectroscopy[4–6]. This non-equilibrium phase seems to be induced by low current densities, but its role in the current-driven IMT remains elusive. Another major hurdle is the pronounced structural transition accompanying the IMT, in which the RuO_2 octahedra are elongated, and the unit cell is transformed from orthorhombic to tetragonal[3–5, 7, 17, 28, 29]. This transition leads to a strong temperature dependence of the unit cell volume (~1% between 100 K and 400 K), introducing large internal strains in the crystal, often resulting in the formation of cracks or even shattering the crystal upon reentering the insulating phase[28].

Although it is much debated whether the IMT is primarily triggered by Joule heating or driven by electronic effects, a parameter that has been left unexplored in this discussion is the size of the samples. Decreasing the size of bulk samples down to µm range gives considerably more control over current paths in the crystal (due to the uniform rectangular cross section). Furthermore, micro cracks and step-like terraced edges, which occur naturally in mm-sized bulk crystals, are scarce in microscopic samples. Also, since the voltage contacts cover the entire side of the microscopic samples, the current injection is more homogeneous. This contrasts with mm-sized crystals where point contacts, and their entailing current crowding effects, are more common. Finally, the microscopic samples are expected to be less susceptible to thermal gradients and heating effects due to the enhancement of the surface-to-volume ratio and the direct contact with an isothermal substrate.

In this chapter, we carry out an extensive size-dependent study using a large number (39) of ultra-pure single crystal samples of Ca_2RuO_4, ranging between the hundreds of nm and the millimeter scale. We examine the role of the current density in inducing the non-equilibrium phase, which we can probe reversibly (i.e., without inducing the IMT and consequently damaging or altering the crystal). Upon decreasing the cross section, we find a dramatic enhancement of the required current density by at least four orders of magnitude. Furthermore, by integrating a micrometer-sized platinum thermometer, we are able to directly probe the local temperature of the microscopic samples, and demonstrate that the pronounced size dependence is not caused by thermal effects. Our findings call for a careful reexamination of the relevant mechanism behind the non-equilibrium phase and its relation to the IMT in Ca_2RuO_4.

6.2. CHARACTERIZING MICROSCOPIC SAMPLES

To examine the crossover from mm-sized bulk behavior to the microscopic one, we have produced samples of varying cross section between 0.5 mm^2 and 0.5 µm^2. The microscopic samples were fabricated using mechanical exfoliation[30, 31]. This enables us to produce micron-sized "crystal flakes," which can be lithographically contacted for electrical transport measurements without compromising the material quality. In addition to the microscopic samples, we have fabricated mm-sized bulk samples that are hand-contacted by using silver paint. We employed a focused Ga^+-ion beam (FIB) to control the cross section systematically. Figures 6.1a and 6.1b show scanning electron microscope and optical microscope images of samples in microscopic and mm-sized ranges, respectively. In Appendix A the sample fabrication is further detailed.

All measurements are carried out by biasing a current in the ab-plane rather than a voltage since inducing the metallic state by applying an electric field is more abrupt, and therefore the crystals are more likely to break. Furthermore, the current density as a function of electric field is hysteretic, complicating the study of size effects. We have conducted electric field versus current density (JE-characteristic) and resistivity as a function of temperature measurements and found that the microscopic samples qualitatively show similar behavior as the mm-sized bulk samples[4]. Typical results obtained on microscopic samples are summarized in Figures 6.1c and 6.1d. It is important to note that, despite several orders of magnitude of size variation, we find the room temperature resistivity of all our samples (microscopic and mm-sized bulk) to be comparable and in good agreement with the literature values[1]. Curiously, however, the temperature-induced IMT is broadened in microscopic samples with respect to those observed in mm-sized bulk samples (see Figure 6.1d). We attribute the broadening of the transition to the small sample thickness since similar effects are observed in thin film samples[32–35]. We did observe an abrupt change in resistivity upon cooling a relatively thick (0.5 µm) microscopic sample through the metal to insulator transition for further discussion on this aspect the reader is referred to Appendix B.

6.3. COMPARING SAMPLES OF DIFFERENT CROSS SECTION

Figure 6.1c shows JE-characteristics obtained on a microscopic sample at different temperatures. These curves qualitatively show similar behavior as the mm-sized bulk samples. However, the current density required for triggering the metastable phase, which is indicated by a negative $\mathrm{d}E/\mathrm{d}J$ as a function of J, exceeds the literature values (for mm-sized crystals) by at least four orders of magnitude[7, 17, 23]. This is demonstrated in Figure 6.2, where we plot the differential resistivity $\mathrm{d}E/\mathrm{d}J$ as a function of J for selected samples. The current density at which $\mathrm{d}E/\mathrm{d}J$ begins to decline, corresponding to nonlinear conduction, increases if the sample size is reduced to microscopic scales. In order to compare the nonlinear conduction under applied current between different samples in a systematic manner, we propose a Figure of Merit (FOM) that can be applied to samples of different sizes. First, differential resistivity versus current density curves are computed by analytically differentiating the JE-characteristics (upper panel of Figure 6.2). The curves are then normalized to their low current value (i.e., currents for which the resistivity is current independent; the lower panel of Figure 6.2). Next, we choose the current density at which the slope of the JE-curve has halved as our Figure of Merit, called the 50%-slope current density. The choice for this FOM is suitable since we can compare the size dependence of the JE-characteristics in a regime where heating effects play a relatively unimportant role. Furthermore, at the FOM current density, the metallic phase is not yet induced in the sample[4]. However, the shape of the JE-curves is the same between all measured samples. This means that the current density at which the metallic phase is induced scales with the FOM. Therefore, the FOM allows us to make a prediction of the metastable and metallic phases. Lastly, the slope of the differential resistivity appears to be maximal at the FOM. Therefore, the choice of this FOM leads to a small uncertainty in the estimated current density, which is not the case when using the current density at the maximum E-field, for

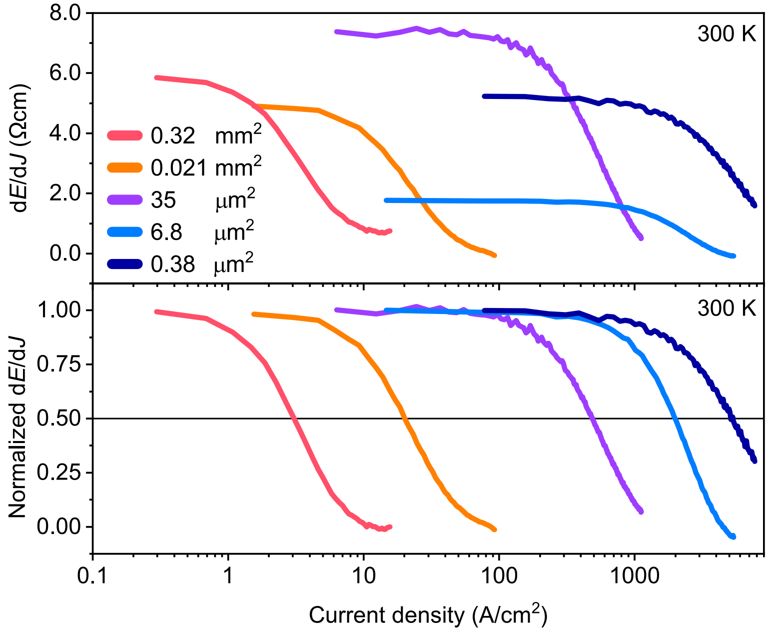

Figure 6.2: The top panel shows the differential resistivity dE/dJ as a function of current density of a few selected samples at room temperature. The legend shows the cross-sectional area of these samples. For all microscopic and mm-sized bulk samples, the low current resistivity at room temperature corresponds to the literature values. In the lower panel, the differential resistivity of these samples is normalized with respect to the low current resistivity (i.e., where the resistivity is current independent). Even though the JE-characteristics of all samples are qualitatively the same, the current density scale at which they exhibit non-linear conduction differs orders of magnitude. The current density at which the slope of the JE-characteristic is halved is chosen as the Figure of Merit (FOM). We show the FOM by the horizontal reference line in the lower panel.

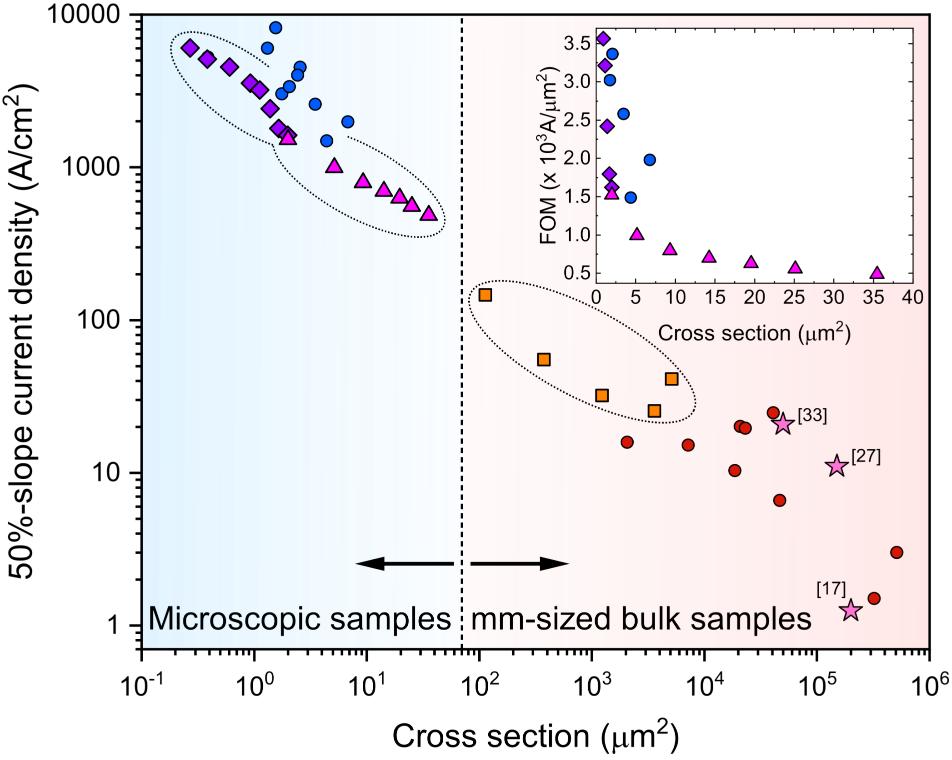

Figure 6.3: The FOM as a function of cross-sectional area for all measured samples at room temperature on a log-log scale. N.B. each data point corresponds to a single sample. The thinning study samples are depicted with a unique non-circular symbol and a different color. The inset displays the FOM vs sample cross section for selected samples on linear scales. The star-symbols correspond to the FOM extracted from literature; the label indicates the reference number.

instance.

Figure 6.3 displays the FOM as a function of the sample cross section for all measured samples. The current density required for nonlinear conduction grows monotonically with decreasing sample dimensions, and the FOM shows a power law dependence on the cross-sectional area. To exclude any potential artifacts associated with sample preparation, we performed a thinning study on three samples over an extensive size range. We incrementally modify the width and thickness of the same crystal through consecutive FIB structuring steps and measure the JE-characteristic, after each one. Following this procedure, we changed the width of a single microscopic sample during up to seven different thinning steps. Moreover, in an mm-sized bulk sample, we decreased the sample width by a factor of 50. Samples on which a thinning experiment is carried out are encircled and highlighted in Figure 6.3 by a non-circular symbol and a different color. Scanning electron micrographs of these samples are shown in Figure 6.4. The FOM as a function of only the width or thickness of the sample (see Appendix

C) reveals the size dependence is not exclusively formed by any of these two parameters but is instead a combination between them, which means that neither of these dimensions is more significant in determining the transport properties of the crystal. The cross section is the most straightforward combination of the two parameters, which is chosen in Figure 6.3.

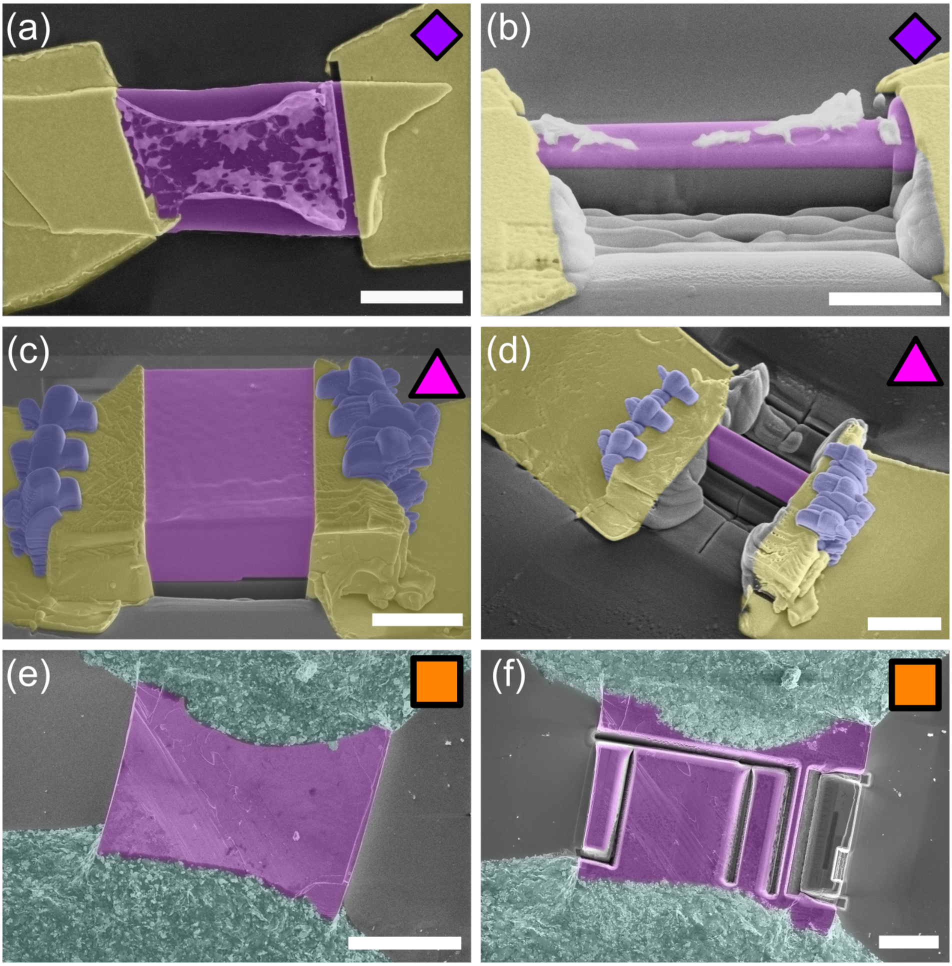

Figure 6.4: False colored scanning electron micrographs of samples used for the thinning experiment in different stages of thinning. In all images, purple indicates the crystal, and yellow indicates titanium/gold contacts to the sample. (a) and (b) correspond to the sample indicated by diamond signs in Figure 6.3. It covers the smallest size ranges; the scale bars correspond to 3 μm and 2 μm, respectively. Some lithography resist residue can be observed in white. The sample depicted in (c) and (d) covers the intermediate sizes (scale bars are respectively 4 μm and 5 μm long) and is represented by triangles in 6.3. Indicated in blue is the electron beam induced deposited tungsten used to strengthen the contacts to the crystal. The third sample of the thinning study is shown in images (e) and (f). It is a relatively small mm-sized bulk sample contacted using silver epoxy (false colored in light blue). Orange squares depict the FOM data of this sample in 6.3. The scale bars in these images represent 100 μm and 50 μm, respectively.

Despite the clear trend in Figure 6.3, there is a sample-to-sample variation that cannot be explained by the uncertainty in the measured crystal dimensions. The deviation from the trend in the mm-sized samples can be explained by irregular current paths in the sample and inconstant cross-sectional area throughout the length of the sample. For the microscopic samples, this does not hold. However, the ratio between width and thickness differs among the samples, and therefore they are expected to respond differently to decreasing dimensions if surface layer effects are important. Furthermore, oxygen relocation can modify the crystal structure when passing a current, resulting in a change of transport properties between current cycles. This is consistent with our observations, where, in some cases, the JE-characteristic slightly changes after different current or temperature cycles. These arguments explain the increased spread observed in Figure 6.3.

6.4. THE ROLE OF TEMPERATURE

Measuring the local sample temperature proved to be vital in many proceeding studies[7, 18, 23–27]. These experiments, where the temperature is locally measured in Ca_2RuO_4, are carried out on mm-sized bulk samples using optical techniques, as local contact thermometry is experimentally challenging to realize at these dimensions. On the other hand, microscopic samples do not have this limitation and enable contact thermometry to give insight into the local sample temperature. This section describes measurements acquired using such a thermometer, accompanied by thermal simulations.

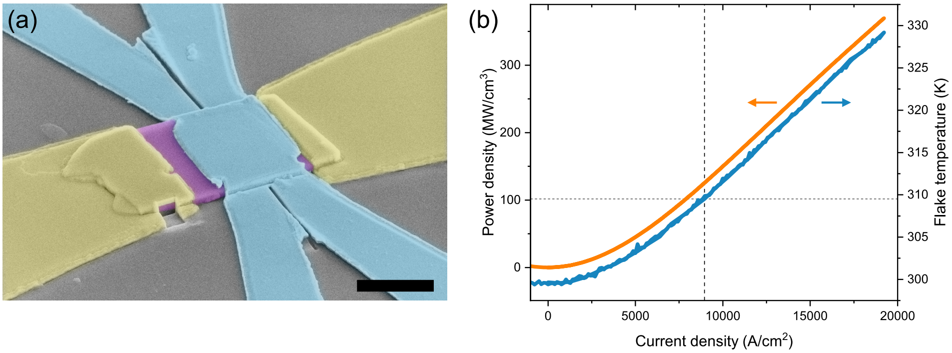

Figure 6.5: (a) Displays a false colored scanning electron micrograph of a microscopic sample (purple) with, in blue, the embedded Pt-thermometer, which can be employed to locally measure the temperature. The yellow parts are the Ti/Au contacts. This is the same sample as depicted in Figure 6.1a; it has a cross-sectional area of 1.6 μm^2 and the scale bar represents 3 μm. (b) displays the measured power density calculated by multiplying the current density by the electric field, depicted with the measured local sample temperature. There is a one-to-one correspondence of the local temperature to the power density, indicating that the temperature increase is due to Joule heating. The dissipated power is used as input data for the simulations (see section 6.4.2).

6.4.1. MICRO-SCALE THERMOMETRY

We designed and fabricated a platinum thermometer on top of selected microscopic samples. Since platinum has a linear temperature dependence, we can accurately measure the temperature of the microscopic samples while simultaneously driving a current using an independent bias. The full details on the fabrication of the Pt-thermometer are provided in Appendix A. Figure 6.5a shows a false colored scanning electron micrograph of the same sample depicted in Figure 6.1a, after the deposition of the Pt-thermometer. We calculate the power density dissipated in the sample by multiplying the measured electric field by the applied current density. In Figure 6.5b, we plot this quantity along with the measured local sample temperature. The shapes of the two curves match closely, which gives a strong indication that we are measuring the temperature increase caused by Joule heating. Note that at the FOM current density, the locally measured temperature increase is less than 10 K. Therefore, we conclude that Joule heating is non-zero but similar to mm-sized bulk samples[23].

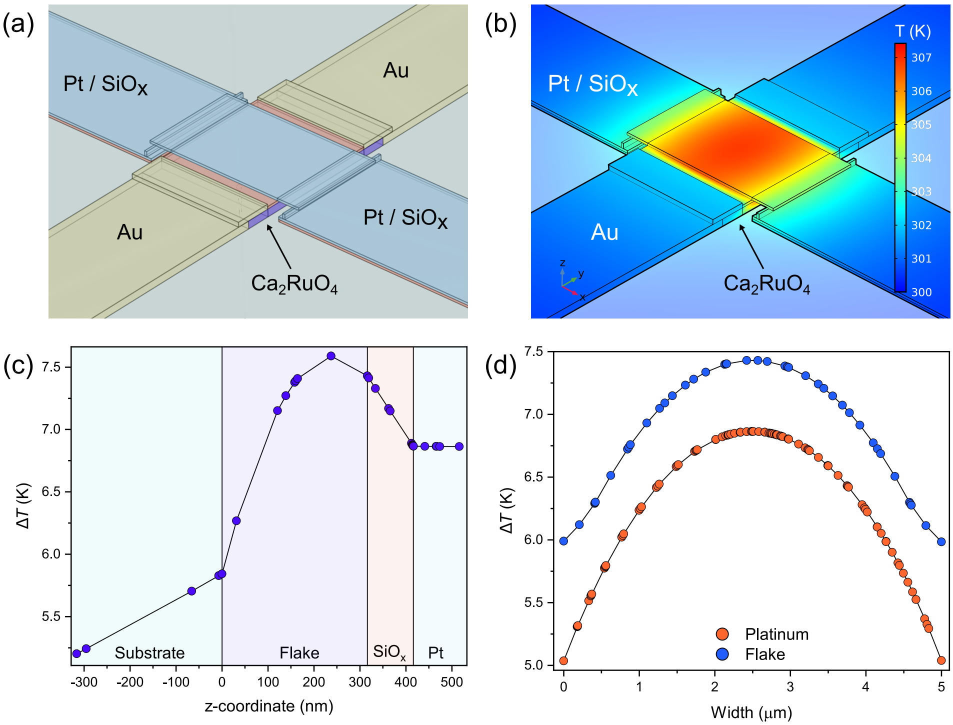

Figure 6.6: (a) Shows a schematic overview of the different elements simulated. Each color corresponds to the labeled material. In (b) the simulated surface temperature heatmap of the sample in (a) is depicted. (c) depicts the temperature increase $\Delta T = T_{\text{flake}} - 300$ K along a vertical line cut through the center of the substrate, flake and thermometer. The different parts of the sample are labeled by the same colors as in (a). The simulated temperature along a horizontal line parallel to the Pt-thermometer leads is displayed in (d). The temperature in **a,b** and (c) is evaluated at the FOM current density.

6.4.2. COMSOL SIMULATIONS

In order to verify that the temperature difference between the Pt-thermometer and the sample is negligible and to investigate the likelihood of any potential temperature gradients in the sample, we have performed thermal simulations supporting the thermometry results. We consider the geometry displayed in Figure 6.6a, which is a true-to-size model of the sample shown in Figure 6.5a. We solve for a steady-state temperature under the assumption that heat is generated uniformly in the part of the crystal between the gold contacts (i.e., not in the parts covered by gold), while the substrate temperature remains constant, 50 µm away from the sample. As input power, we use the measured power density displayed in Figure 6.5b. The temperature equilibrium is governed by the thermal conductivity of the materials, which Terasaki et al. have evaluated for Ca_2RuO_4 to be 5.1 W/mK and 1.8 W/mK for in- and out-of-ab-plane, respectively[26]. The resulting surface temperature distribution is shown in Figure 6.6b.

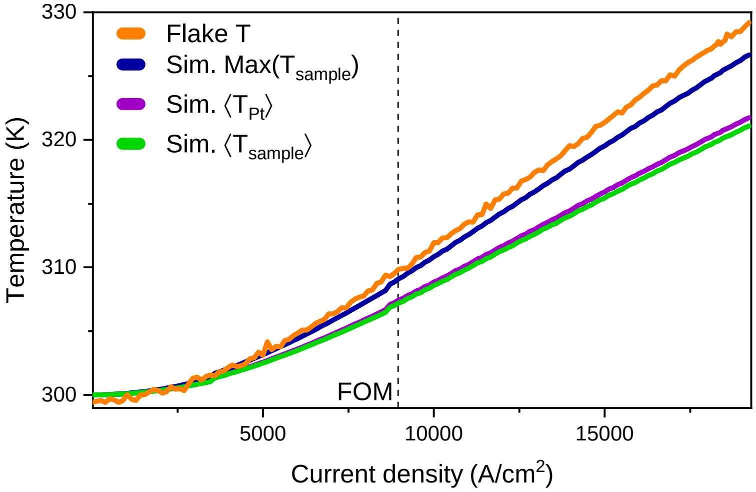

Figure 6.7: The local measured Pt temperature compared to multiple simulated temperatures as a function of the applied J. The data is acquired on the sample depicted in Figure 6.5a. The substrate temperature is 300 K, and The vertical reference line indicates the FOM. The simulated average sample (green curve) and Pt temperature (purple curve) correspond to a high degree, which leads to the conclusion that the Pt-thermometry technique is suited for establishing the sample temperature. The difference between the measured and simulated temperature can be caused by the absence of heat transfer barriers in the simulations.

Figure 6.6c and 6.6d show the temperature variations within the sample at the FOM current density. Here, the temperature increase is plotted as a function of a vertical and horizontal line cut, respectively. The temperature increases roughly quadratically from the sides of the crystal towards the hottest point of the flake. The temperature variations in the flake were found to be lower than 3 K at the FOM current density.

In Figure 6.7 we compare the platinum thermometry data to the simulation results. The measured temperature (orange) exceeds the expected averaged Pt temperature (purple). This can be caused by the absence of heat transfer barriers between the simulated elements. On the other hand, these can be expected in experiments. The purple curve can therefore be considered a lower bound of the expected Pt temperature. Nevertheless, the simulated average sample (green) and Pt temperature (purple) show correspondence to a high degree. We also evaluate the maximum temperature within the simulated flake geometry (blue curve) and compare it to the simulated average Pt temperature, which we find to differ less than 2 K at the FOM current density. Therefore, we consider our Pt thermometry technique suited for acquiring the average sample temperature at the FOM.

6.4.3. CONSEQUENCES OF HEATING

The measurement of the local temperature enables us to calculate what the JE-characteristic would look like based on heating effects only. For the resistivity versus temperature measurement on this sample, we compute the $\mathrm{d}E/\mathrm{d}J$ from our JE-characteristics for low currents (i.e., where the resistivity ρ is current independent):

$$\rho(T) = \frac{\mathrm{d}E}{\mathrm{d}J}(T, J \approx 0) \tag{6.1}$$

Since the temperature is homogeneous up to a variation of 3 K over the entire sample, we can use the locally measured temperature as a function of current density to find the $\mathrm{d}E/\mathrm{d}J$ as a function of heating effects:

$$\frac{\mathrm{d}E_{\mathrm{thermal}}}{\mathrm{d}J}(J) = \frac{\mathrm{d}E}{\mathrm{d}J}(T(J), J \approx 0) = \rho(T(J)) \tag{6.2}$$

Integrating the equation (6.2), we can reconstruct the JE-characteristic that would result, if Joule heating would be the only mechanism causing nonlinear conduction. We set the integration constant by requiring zero electric field for zero current density ($E(0) = 0$; see Appendix D for more details):

$$E_{\mathrm{thermal}}(J) = \int \frac{\mathrm{d}E_{\mathrm{thermal}}}{\mathrm{d}J}(J)\mathrm{d}J \tag{6.3}$$

We denote this reconstructed function as $E_{\mathrm{thermal}}(J)$ and plot it alongside the measured data in Figure 6.8a. Even at low current densities, the actual measured data shows stronger nonlinear conduction than $E_{\mathrm{thermal}}(J)$, indicating that current-driven effects are significant in the microscopic samples for all applied current densities probed in this study.

Alternatively, the differential resistivity as a function of local sample temperature is plotted in Figure 6.8b. The purple curve describes the resistivity as a function of temperature with a constant current density (62 A/cm^2). Alongside, we plot the differential resistivity as a function of increasing bias current while maintaining a constant substrate temperature. The slope decrease of JE-characteristic, caused by the application of current, is not exclusively driven by Joule heating.

Based on our simulations and thermometry experiments, we conclude that the size dependence presented in Figure 6.3 cannot be explained by Joule heating. Furthermore, we find that a current-driven mechanism is present parallel to heating effects in the non-equilibrium phase.

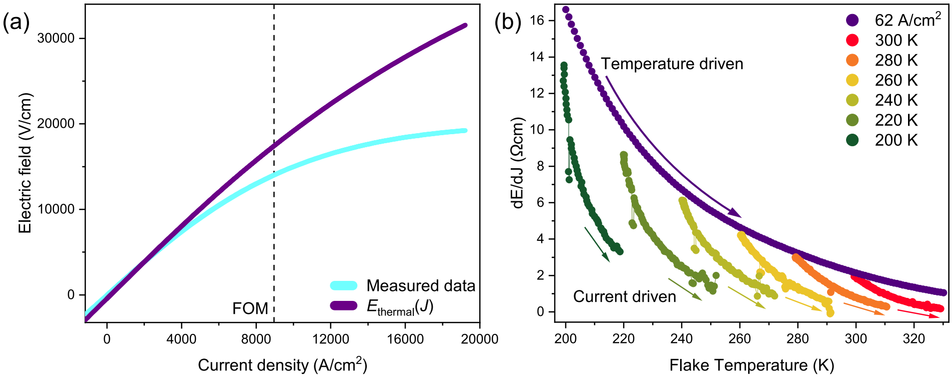

Figure 6.8: (a) shows the electric field acquired simultaneously with the temperature measurement of Figure 6.5. The measured data is compared to E_{thermal}, which is the calculated electric field on basis of Joule heating only. The vertical reference line indicates the FOM. Alternatively, (b) displays the differential resistivity as a function of the flake temperature. Either the substrate temperature (purple) or the current density is changed. At all current densities, the nonlinear conduction is stronger than heating effects can provide.

6.5. DISCUSSION

Before discussing the possible origin of the observed size dependence, we consider the following notes. Firstly, there seems to be no intrinsic length scale found in our measurements. This can be seen from the absence of a specific cross section where the FOM changes discontinuously. Secondly, we can exclude the effects of microcracks since the size dependence continues even in the microscopic regime where micro cracks are not present. By inspecting the samples with a scanning electron microscope, we could confirm that no micro cracks were induced by measuring the JE-characteristic. Thirdly, Jenni et al. observed a similar current-driven mechanism parallel to Joule heating, as is reported here[24]. Lastly, we note that our findings are consistent with the reports on epitaxially grown thin films of Ca_2RuO_4, where the current density required to induce the IMT was also found to be many orders of magnitude higher than in bulk literature values[32].

The emergence of the metallic phase was recently attributed by Terasaki et al[26]. to energy flow, as opposed to charge transport. In this study, the energy flow corresponds to the dissipated power (product of current and voltage IV). In contrast, it is more insightful to describe the product of electric field and current density EJ (power dissipation density), enabling the comparison of samples of different length scales. Since microscopic samples show a four order of magnitude increase in current density at which we observe nonlinear transport, we find that the power dissipation density is eight orders of magnitude larger in microscopic samples than in mm-sized bulk samples (see Figure 6.5a). Therefore, it is unlikely that the energy flux through the crystal is responsible for the observed size dependence.

Alternatively, strain, induced through coupling to the substrate, might explain the size dependence. In the zero-current limit, however, the substrate does not exercise any strain on the crystal, as we will discuss below. The room temperature resistivity of Ca_2RuO_4 strongly depends on strain, and the IMT can be induced by applying 0.5 GPa of pressure[3, 13, 14]. By using ultra-low currents ($\backsim$nA), we have confirmed that the insulating-state resistivity of the microscopic samples matches that of their mm-sized counterparts, signaling the absence of strain. Moreover, as discussed in Chapter 7, we have prepared microscopic samples using equal methods and substrates on isostructural Sr_2RuO_4. These samples retained bulk properties to sizes below 200 nm, whereas, like Ca_2RuO_4, its transport properties depend heavily on strain[36–38]. Therefore, we conclude that our microscopic samples do not experience strain at zero current bias. In simultaneous transport and X-ray diffraction measurements, it has been shown that there is no detectable change of the lattice parameters at the FOM current density[4]. Combined with the absence of strain at zero current bias, this leads to the conclusion that our samples do not experience any strain at the FOM, regardless of their size. Thus, we do not regard strain as a plausible explanation for the observed size dependence.

Near the IMT, independent of whether it is induced by current or temperature, the arguments supporting the absence of strain no longer hold, as the lattice constants significantly alter[4, 5]. Although we are far below the IMT in our current-driven experiments, we pass the IMT in the temperature sweep, presented in Figure 6.1d. Strain-related effects could be responsible for the observed broadening of the transition. Moreover, a broadened transition is commonly observed in thin films, where strain induced by the substrate is expected to be an influential parameter[32–34].

Finally, an inhomogeneous current distribution throughout the cross-sectional area could potentially explain the size dependence. Since the current density is calculated by dividing the applied current by the entire cross section, the *apparent current den-*

sity in mm-sized bulk samples might be lower than the *actual current density*, which is physically relevant. When sample dimensions are reduced, however, the apparent and actual current densities can be more similar, and therefore we might measure an increase in apparent current density.

Metallic filament formation, known to occur in Mott insulators, can be the origin of such highly inhomogeneous current distributions[39]. Contrarily, for Ca_2RuO_4, Zhang et al. inspected phase separation using scanning near field optical microscopy (SNOM) and found a ripple pattern at the phase boundary between the insulating and metallic states[7]. Although the resolution of the SNOM technique might be insufficient to rule out sub 100 nm channel formation, it is difficult to reconcile the striped pattern found in SNOM with filament formation at present.

On the other hand, Zhang et al. find that the metallic phase nucleates at the top of the sample, and its depth increases when traversing a phase boundary in the phase-separated state. This could suggest an inhomogeneous current distribution throughout the cross-sectional area (high at the edges of the crystal and decreasing towards the center of the bulk). Since the microscopic crystals have a larger surface-to-volume ratio, the edges are relatively more dominant. If the current density gradually increases below the current-carrying surface, this proposed mechanism will not feature any length scale at which a discontinuous change is expected in the FOM, which is compatible with our findings. In Appendix E, a minimal toy model describing the inhomogeneous current density is presented. This model can reproduce the power law dependence observed in Figure 6.3.

6.6. CONCLUSION

In conclusion, we have performed a detailed study on the size-dependent electrical properties of the Mott insulator Ca_2RuO_4. We find a surprising relation between crystal size and the current density at which nonlinear conduction occurs, which increases four orders of magnitude when the sample size is reduced from 0.5 mm^2 to 0.5 $\mu\mathrm{m}^2$. We have strong indications that the observed size dependence is not caused by Joule heating, using a local Pt-thermometer fabricated on top of selected microscopic samples. Our findings indicate an intrinsically inhomogeneous current density distribution in single crystals of Ca_2RuO_4. This calls for a reexamination of the relevant role of charge current in the metastable phase and its possible relation to the IMT. As an outlook, the combination of microscopic samples with a well-controlled current path, and local platinum temperature probes, provides a state-of-the-art approach to study the interplay between thermal and electronic effects, which can be used to study the IMT in Mott insulators.

APPENDICES

A. CRYSTAL GROWTH AND SAMPLE FABRICATION

Bulk single crystals of Ca_2RuO_4 were grown using a flux-feeding floating zone technique with Ru self-flux using a commercial image furnace equipped with double elliptical mirrors. Several techniques, including X-ray diffraction, energy dispersive spectroscopy, and polarized light optical microscopy analysis, have been used to fully characterize the structure, quality, and purity of the crystals. See references [40] and [41] for further details.

The microscopic samples were fabricated using mechanical exfoliation on highly resistive $SrTiO_3$ or sapphire substrates[31]. The flake samples are significantly thicker than monolayers. Therefore, random strain patterns, wrinkles, and folds associated with the thin film limit are absent. Due to the natural shape of the crystal flakes, the produced samples are suited best for passing current in the ab-plane. Therefore all experiments are carried out in this configuration.

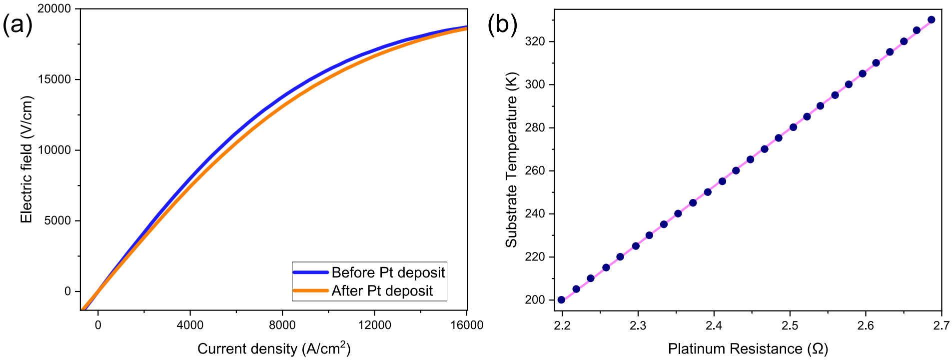

Figure A.1: (a) Displays the JE-characteristic before and after the deposition of the Pt-thermometer on the sample depicted in Figure 6.5a. In (b) the calibration curve of the Pt-thermometer, which is fitted by a linear curve, is shown. The slope of the fit corresponds to 0.27 K per mΩ. This enables sub-Kelvin precision thermometry.

Considerable effort is put into the fabrication of the electrical connections on the samples to reduce the contact resistance that possibly becomes an extrinsic origin for nonlinear conduction due to local Joule heating. In order to perform electrical transport measurements, the samples obtained by the exfoliation process were contacted using electron beam lithography designed and sputter-deposited Ti/Au contacts. When necessary, we used electron beam induced deposition to provide an electrical reinforcement of the contacts by locally depositing an additional layer of tungsten-carbide on them. In addition to the microscopic samples, we have fabricated conventionally mm-sized bulk samples that are contacted by hand using silver paint (Agar Scientific G3691). On the mm-sized samples, we found a resistive background in the JE-characteristics, from which we extracted the contact resistance to be less than 10

Ω, which is significantly smaller than the sample resistance, supporting the use of a two-probe measurement. In addition, some microscopic samples were contacted in a 4-probe geometry. Using these samples, we could confirm that the contact resistance is negligible compared to the sample resistance.

We used the FIB technique to modify the sample width and thickness, enabling full control of sample dimensions and geometry over an extensive crystal size range. An often-heard criticism of FIB processing is the implantation of Ga-ions and damage induced to the crystal due to the high impulse of the ions. The key to resolving these issues is the combination of ultra-low beam currents and an SiO_x capping layer. The first ensures that the damages are only very local (approximately 30 nm from the edge of the milled structure), and the second protects the top side of the crystal during the inevitable radiation of Ga-ions.

The Pt-thermometer is added to selected samples in a second step of electron beam lithography. The Pt-circuit is electrically isolated by a thin layer of sputter-deposited SiO_x (~ 100 nm). This ensures that the Pt-thermometer and sample form two decoupled electrical systems. The resistance between the Pt-circuit and the Ca_2RuO_4 crystal is over 1 GΩ. Besides, the application of the thermometer does not affect the JE-characteristic (see Figure A.1a). The thickness of the SiO_x layer is optimized, providing a disconnected electrical system from the crystal while remaining in thermal contact to provide sub-Kelvin measurement precision. The material of choice for the thermometer circuit is platinum since its resistivity is highly linear over the temperature range at which we carry out our experiments, as seen in the thermometer calibration curve of Figure A.1b. The resistance of the Pt-thermometer changes by 0.27 K/mΩ.

B. ABRUPT TRANSITION IN A RELATIVELY THICK MICROSCOPIC SAMPLE

In most of the microscopic samples, the temperature-driven IMT is broadened. Figure 6.1d shows the general resistivity versus temperature behavior of microscopic samples. However, on one of our microscopic samples with a relatively large thickness (1.5 μm) with respect to the width (3 μm), we have acquired a resistivity versus temperature curve that resembles data acquired on mm-sized bulk crystals (see Figure B.1a): we observe a hysteretic curve that displays an abrupt transition upon cooling through the MIT. N.B., the other transport properties of this sample are fully resembling a typical microscopic sample, including a high Figure of Merit current density. A false colored scanning electron micrograph of this sample is found in Figure B.1b.

A possible origin of the observed broadening of the transition might be strain patterns in the sample caused by the coupling to the substrate. While driving low currents (current densities well below the IMT; including the FOM), our microscopic samples do not experience any strain. However, near the IMT - independent of whether it is induced by current or temperature - this no longer holds, as the lattice constants significantly alter and strain effect can dominate[4, 5]. Furthermore, a broadening of the transition is commonly observed in thin films, where strain caused by the substrate is a crucial parameter[32–34].

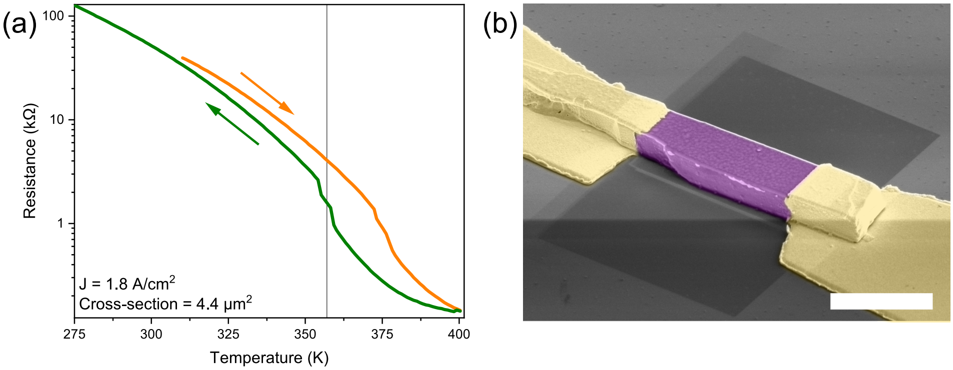

Figure B.1: (a) Shows the resistance versus temperature of a microscopic sample that is 1.5 µm thick and 3 µm wide, which is relatively thick for a sample in the microscopic size range. We observe hysteresis on cycling the temperature and see an abrupt change in resistance when passing the thermal transition temperature of 357K, as indicated by the vertical reference line. In (b), a false colored scanning electron micrograph is shown of the sample used to gather data in Figure (a). Purple indicates the crystal and yellow colored are the titanium/gold contacts. The scale bar corresponds to 5 µm.

C. THE FIGURE OF MERIT AS A FUNCTION OF OTHER LENGTH SCALES

In Figure 6.3, we have chosen to plot the Figure of Merit as a function of the cross-sectional area. Here we present the same data as a function of thickness, width, and length (between the voltage contacts) of the crystal, as plotted in Figure C.1. Most interesting are the samples on which we have performed a thinning study, highlighted by the use of a non-circular symbol in Figure C.1. For the samples of constant thickness, we observe that the FOM can change an order of magnitude in a single sample while decreasing the width, which rules out a dependence solely on thickness. A similar argument can be made for the width and length dependence. Indeed, we have carried out a single step of decreasing the thickness of a sample, which is indicated by the use of arrows in Figure C.1. While the width is constant, the Figure of Merit changes again if we decrease the thickness of this sample.

If we, however, plot the Figure of Merit as a function of the cross-sectional area of the sample, as is done in Figure 6.3, we find that the thinning study samples follow a more coherent trend. Therefore, we use the cross-section as a typical length scale measure. We can conclude from this observation that neither thickness, width, nor length of the crystal solely governs the Figure of Merit, meaning that none of these dimensions are more critical in determining the transport properties of the crystal.

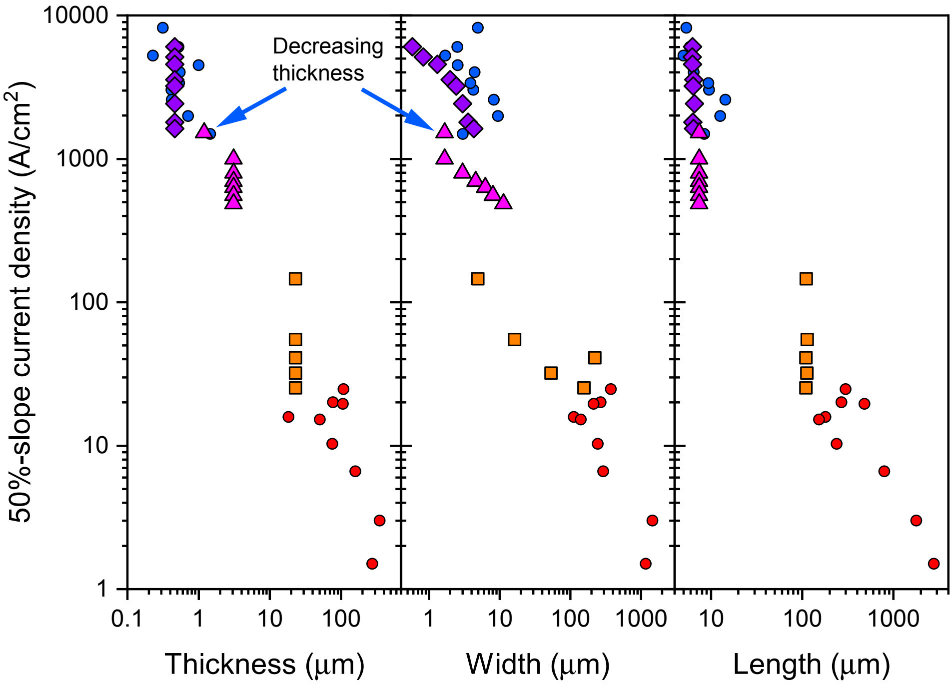

Figure C.1: the 50%-slope current density (FOM) shown as a function of different length scale parameters of the measured samples. In this Figure, each data point represents a single sample. The non-circular symbols represent the thinning study samples (see Figure 6.4 for images of these). The arrows indicate the decrease of thickness during the thinning study on the sample depicted in Figure 6.4c and 6.4d.

D. RECONSTRUCTING THE JE-CHARACTERISTIC ON BASIS OF JOULE HEATING ONLY

Using analytical differentiation it is possible to calculate $\mathrm{d}E/\mathrm{d}J$ from $E(J)$. Reversely, one can calculate $E(J)$ by integration of $\mathrm{d}E/\mathrm{d}J$. The latter introduces an integration constant that needs to be set by a boundary condition. The boundary condition in our case is the requirement of zero electric field for zero current density: $E(0) = 0$. To summarize:

$$E(J) \xrightarrow{\text{diff.}} \frac{\mathrm{d}E}{\mathrm{d}J}(J) \xrightarrow{\text{int.}} E_{\text{recon.}}(J) + C_{\text{int.}} \xrightarrow{\text{Boundary condition}} E_{\text{recon.}}(J) = E(J) \qquad (6.4)$$

Here $C_{\text{int.}}$ is the integration constant and $E_{\text{recon.}}$ is the reconstructed electric field from the derivative $\mathrm{d}E/\mathrm{d}J$. As a sanity check, we perform differentiation and integration sequentially on acquired electric field and recover the originally measured data (see Figure D.1a).

The resistivity as a function of temperature is measured by calculating the slope of the

JE-characteristic for low currents (i.e., here, the slope of $E(J)$ is current independent, and no local temperature increase is measured). We can therefore interchange the resistivity as a function of temperature for the $\mathrm{d}E/\mathrm{d}J$ as a function of temperature at approximately zero applied current:

$$\rho(T) = \frac{\mathrm{d}E}{\mathrm{d}J}(T, J \approx 0) \tag{6.5}$$

The application of the Pt-thermometer allows us to measure the local absolute temperature as a function of the current density in the sample. When the crystal temperature increases, the resistivity lowers, causing a decrease of $\mathrm{d}E/\mathrm{d}J$ and, therefore, a decline of the slope of the JE-characteristic. Since we have both the $\mathrm{d}E/\mathrm{d}J$ as a function of temperature and the temperature as a function of current density available, we can combine these to find the $\mathrm{d}E/\mathrm{d}J$ as a function of the locally measured temperature

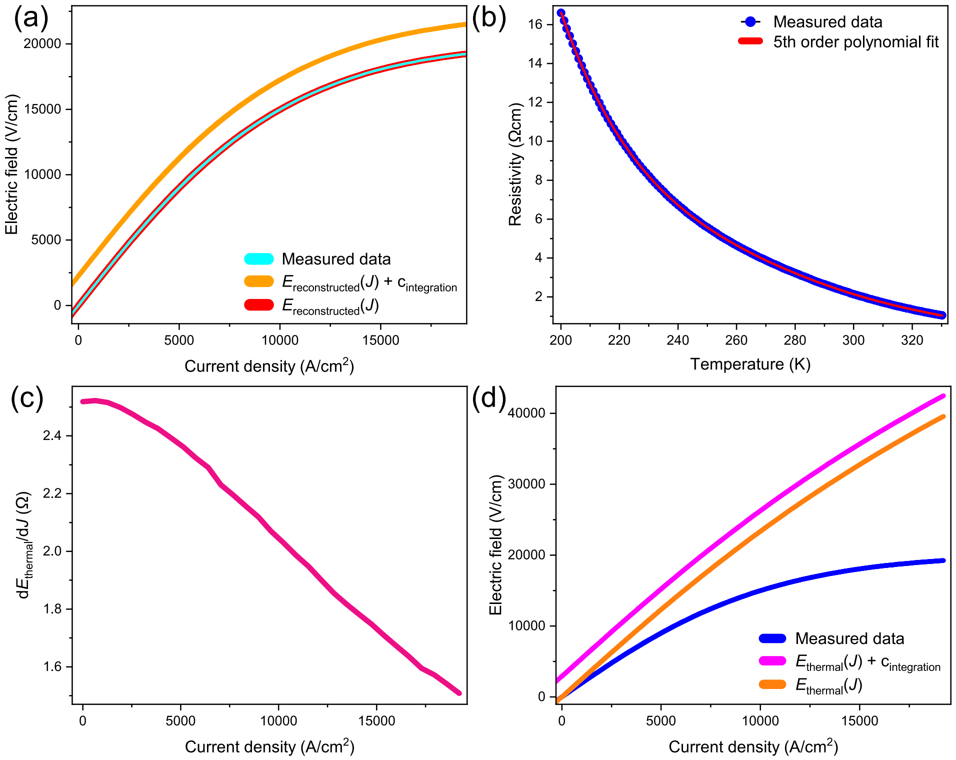

Figure D.1: Summary of calculating E_{thermal}. As a sanity check, we perform subsequent differentiation and integration of a dataset and retrieve the original measured data, which is depicted in (a). (b) shows the resistivity versus temperature curve measured on a sample with embedded Pt-thermometer. The data is fitted by a 5th order polynomial to capture its phenomenological behavior. This fit is used to find the $\mathrm{d}E_{\text{thermal}}/\mathrm{d}J(J)$ (shown in (c)), which is integrated to retrieve E_{thermal} (shown in (d) and Figure 6.8b).

caused by the application of current density, which we denote as $\mathrm{d}E_{\text{thermal}}/\mathrm{d}J$:

$$\frac{\mathrm{d}E}{\mathrm{d}J}(T, J \approx 0)\ \&\ T(J) \xrightarrow{\textit{substitution}} \mathrm{d}E_{\text{thermal}}/\mathrm{d}J(J) \tag{6.6}$$

To make this substitution, we fit the measured resistivity as a function of temperature with a 5th order polynomial to capture its phenomenological behavior (see Figure D.1b). Next, we use the fitted function to calculate $\mathrm{d}E_{\text{thermal}}/\mathrm{d}J$, which is depicted in Figure D.1c. Finally, we apply the above described procedure to reconstruct E_{thermal} using integration, yielding the data that is shown in Figure 6.8b and Figure D.1d.

E. MINIMAL MODEL FOR CURRENT DENSITY INHOMOGENEITY OVER THE CROSS-SECTIONAL AREA

The cross section dependence might be explained by an inhomogeneous current density distribution throughout the cross-sectional area. Here we present a minimal toy model and phenomenologically compare it to the measured data.

Crucial in this analysis is the difference between the *apparent* current density, namely the total current (I) divided by the total cross-sectional area (A):

$$J_{\text{app}} = I/A \tag{6.7}$$

and the *actual* current density that might be dependent on coordinates spanning the cross-sectional area:

$$J_{\text{act}} = \frac{\mathrm{d}I}{\mathrm{d}A}(x, y) \tag{6.8}$$

Where x (y) is a length parameter that runs between $-D/2$ ($-W/2$) and $D/2$ ($W/2$), with D (W) the thickness (width) of the crystal. The actual and apparent current density can be related to each other by integrating the actual current density to find the total current:

$$J_{\text{app}} = I/A = 1/A \iint \frac{\mathrm{d}I}{\mathrm{d}A}(x, y)\mathrm{d}A \tag{6.9}$$

Therefore a homogeneous current distribution (i.e., a constant actual current density) yields an equal apparent current density:

$$J_{\mathrm{act}} = J_0 \rightarrow J_{\mathrm{app}} = 1/A \iint J_0 \mathrm{d}A = \frac{AJ_0}{A} = J_0 = J_{\mathrm{act}} \tag{6.10}$$

We can examine what type of actual current density features the power law dependence on the cross-sectional area observed in the measured current density (displayed in Figure 6.3). To do so, we assume that the actual current density decreases as $J_{\mathrm{act}} = J_0 \lambda^a l^{-a}$. Here a is a dimensionless constant, λ is a characteristic length scale, and l is the distance from the edges of the sample. This means, for a rectangular cross-section, that the total current is given by:

$$I = 4J_0\lambda^a \int_0^{D/2} \int_0^{W/2} \frac{\mathrm{d}I}{\mathrm{d}A}(x,y)\mathrm{d}t\mathrm{d}w \tag{6.11}$$

Here, we used the fact that the system is symmetric in four sectors. Each of those can be divided into two parts:

$$I = 4J_0\lambda^a \left[\int_0^{D/2} \int_0^{\frac{W}{D}x} y^{-a}\mathrm{d}y\mathrm{d}x + \int_0^{W/2} \int_0^{\frac{D}{W}y} x^{-a}\mathrm{d}x\mathrm{d}y \right] \tag{6.12}$$

Leading to:

$$I = \frac{J_0\lambda^a}{(1-a)(2-a)} \left[\left(\frac{D}{W}\right)^{1-a} \left(\frac{W}{2}\right)^{2-a} + \left(\frac{W}{D}\right)^{1-a} \left(\frac{D}{2}\right)^{2-a} \right] \tag{6.13}$$

Where we assumed $a \neq 1$. This can be simplified to:

$$I = \frac{8J_0\lambda^a}{(1-a)(2-a)}(DW)^{1-a} = \frac{8}{(1-a)(2-a)}A^{1-a} \tag{6.14}$$

That entails for the apparent current density:

$$J_{\mathrm{app}} = I/A = \frac{8J_0\lambda^a}{(1-a)(2-a)} \frac{A^{1-a}}{A} = \frac{8J_0\lambda^a}{(1-a)(2-a)} A^{-a} \sim A^{-a} \tag{6.15}$$

Which is the observed power law dependence of the measured current density.

REFERENCES

[1] Nakatsuji, S., Ikeda, S.-i. & Maeno, Y. Ca_2RuO_4: new Mott insulators of layered ruthenate. *J. Phys. Soc. Jpn.* **66**, 1868–1871 (1997).

[2] Alireza, P. L. *et al.* Evidence of superconductivity on the border of quasi-2D ferromagnetism in Ca_2RuO_4 at high pressure. *J. Condens. Matter Phys.* **22**, 052202 (2010).

[3] Nakamura, F. *et al.* From Mott insulator to ferromagnetic metal: A pressure study of Ca_2RuO_4. *Phys. Rev. B* **65**, 220402 (2002).

[4] Cirillo, C. *et al.* Emergence of a metallic metastable phase induced by electrical current in Ca_2RuO_4. *Phys. Rev. B* **100**, 235142 (2019).

[5] Bertinshaw, J. *et al.* Unique crystal structure of Ca_2RuO_4 in the current stabilized semimetallic State. *Phys. Rev. Lett.* **123**, 137204 (2019).

[6] Fürsich, K. *et al.* Raman scattering from current-stabilized nonequilibrium phases in Ca_2RuO_4. *Phys. Rev. B* **100**, 081101 (2019).

[7] Zhang, J. *et al.* Nano-resolved current-induced insulator-metal transition in the Mott insulator Ca_2RuO_4. *Phys. Rev. X* **9**, 011032 (2019).

[8] Alexander, C. S. *et al.* Destruction of the Mott insulating ground state of Ca_2RuO_4 by a structural transition. *Phys. Rev. B* **60**, R8422(R) (1999).

[9] Nakatsuji, S., Ando, T., Mao, Z. & Maeno, Y. Metal–insulator transition in $Ca_{x-2}Sr_xRuO_4$. *Phys. B: Condens. Matter* **259-261**, 949–950 (1999).

[10] Nakatsuji, S. & Maeno, Y. Quasi-two-dimensional Mott transition system $Ca_{x-2}Sr_xRuO_4$. *Phys. Rev. Lett.* **84**, 2666–2669 (2000).

[11] Nakatsuji, S. & Maeno, Y. Synthesis and single-crystal growth of $Ca_{x-2}Sr_xRuO_4$. *J. Solid State Chem.* **156**, 26 – 31 (2001).

[12] Sutter, D. *et al.* Orbitally selective breakdown of Fermi liquid quasiparticles in $Ca_{1.8}Sr_{0.2}RuO_4$. *Phys. Rev. B* **99**, 121115 (2019).

[13] Steffens, P. *et al.* High-pressure diffraction studies on Ca_2RuO_4. *Phys. Rev. B* **72**, 094104 (2005).

[14] Nakamura, F. Pressure-induced Mott transition and related novel quantum phenomena in Ca_2RuO_4. *J. Phys. Soc. Jpn.* **76**, 96–99 (2007).

[15] Braden, M., André, G., Nakatsuji, S. & Maeno, Y. Crystal and magnetic structure of Ca_2RuO_4 magnetoelastic coupling and the metal-insulator transition. *Phys. Rev. B* **58**, 847–861 (1998).

[16] Zegkinoglou, I. *et al.* Orbital ordering transition in Ca_2RuO_4 observed with resonant X-ray diffraction. *Phys. Rev. Lett.* **95**, 136401 (2005).

[17] Nakamura, F. *et al.* Electric-field-induced metal maintained by current of the Mott insulator Ca_2RuO_4. *Sci. Rep.* **3**, 2536 (2013).

[18] Okazaki, R. *et al.* Current-induced gap suppression in the mott insulator Ca_2RuO_4. *J. Phys. Soc. Jpn.* **82**, 103702 (2013).

[19] Taguchi, Y., Matsumoto, T. & Tokura, Y. Dielectric breakdown of one-dimensional Mott insulators Sr_2CuO_3 and $SrCuO_2$. *Phys. Rev. B* **62**, 7015–7018 (2000).

[20] Kanki, T., Kawatani, K., Takami, H. & Tanaka, H. Direct observation of giant metallic domain evolution driven by electric bias in VO_2 thin films on TiO_2(001) substrate. *Appl. Phys. Lett.* **101**, 243118 (2012).

[21] Yang, Z., Ko, C. & Ramanathan, S. Oxide electronics utilizing ultrafast metal-insulator transitions. *Annu. Rev. Mater. Res.* **41**, 337–367 (2011).

[22] Stoliar, P. *et al.* A leaky-integrate-and-fire neuron analog realized with a Mott insulator. *Adv. Funct. Mater.* **27**, 1604740 (2017).

[23] Mattoni, G., Yonezawa, S., Nakamura, F. & Maeno, Y. Role of local temperature in the current-driven metal-insulator transition of Ca_2RuO_4. *Phys. Rev. Mater.* **4**, 114414 (2020).

[24] Jenni, K. *et al.* Evidence for current-induced phase coexistence in Ca_2RuO_4 and its influence on magnetic order. *Phys. Rev. Mater* **4**, 085001 (2020).

[25] Okazaki, R. *et al.* Current-induced giant lattice deformation in the Mott insulator Ca_2RuO_4. *J. Phys. Soc. Jpn.* **89**, 044710 (2020).

[26] Terasaki, I. *et al.* Non-equilibrium steady state in the Mott insulator Ca_2RuO_4. *J. Phys. Soc. Jpn.* **89**, 093707 (2020).

[27] Chiriacò, G. & Millis, A. J. Polarity dependent heating at the phase interface in metal-insulator transitions. *Phys. Rev. B* **102**, 085116 (2020).

[28] Friedt, O. *et al.* Structural and magnetic aspects of the metal-insulator transition in Ca_2RuO_4. *Phys. Rev. B* **63**, 174432 (2001).

[29] Gorelov, E. *et al.* Nature of the Mott transition in Ca_2RuO_4. *Phys. Rev. Lett.* **104**, 226401 (2010).

[30] Huang, Y. *et al.* Reliable exfoliation of large-area high-quality flakes of graphene and other two-dimensional materials. *ACS Nano* **9**, 10612–10620 (2015).

[31] Fermin, R. Fabrication of mesoscopic structures with superconducting Sr_2RuO_4 Master thesis, Universiteit Leiden (2017).

[32] Tsurumaki-Fukuchi, A. *et al.* Stable and tunable current-induced phase transition in epitaxial thin films of Ca_2RuO_4. *ACS Appl. Mater. Interfaces* **12**, 28368–28374 (2020).

[33] Miao, L. *et al.* Itinerant ferromagnetism and geometrically suppressed metal-insulator transition in epitaxial thin films of Ca_2RuO_4. *Appl. Phys. Lett.* **100**, 052401 (2012).

[34] Wang, X., Xin, Y., Stampe, P. A., Kennedy, R. J. & Zheng, J. P. Epitaxial thin film growth of $Ca_2RuO_{4+\delta}$ by pulsed laser deposition. *Appl. Phys. Lett.* **85**, 6146–6148 (2004).

[35] Dietl, C. *et al.* Tailoring the electronic properties of Ca_2RuO_4 via epitaxial strain. *Appl. Phys. Lett.* **112**, 031902 (2018).

[36] Grinenko, V. *et al.* Split superconducting and time-reversal symmetry-breaking transitions in Sr_2RuO_4 under stress. *Nat. Phys.* **17**, 748–754 (2021).

[37] Barber, M. E., Gibbs, A. S., Maeno, Y., Mackenzie, A. P. & Hicks, C. W. Resistivity in the vicinity of a van Hove singularity: Sr_2RuO_4 under uniaxial pressure. *Phys. Rev. Lett.* **120**, 076602 (2018).

[38] Steppke, A. *et al.* Strong peak in Tc of Sr_2RuO_4 under uniaxial pressure. *Science* **355**, eaaf9398 (2017).

[39] Lange, M. *et al.* Imaging of electrothermal filament formation in a Mott insulator. *Phys. Rev. Applied* **16**, 054027 (2021).

[40] Fukazawa, H., Nakatsuji, S. & Maeno, Y. Intrinsic properties of the Mott insulator $Ca_2RuO_{4+\delta}(\delta = 0)$ studied with single crystals. *Phys. B: Condens. Matter* **281-282**, 613–614 (2000).

[41] Granata, V. *et al.* Crystal growth of the Ca_2RuO_4–Ru metal system by the floating-zone technique. *J. Alloys Compd.* **832**, 154890 (2020).